Energy Advances

ROYAL SOCIETY OF CHEMISTRY

PAPER

View Article Online
View Journal

Cite this: DOI: 10.1039/d5ya00191a

$ZnO/Al_2O_3/CuO$ ternary nanocomposites: a bandgap-engineered solution for high-efficiency photocatalytic hydrogen generation

Krishna Daware,[a] Mayuri Khade,[a] Sonali Mhaske,[b] Yogesh Sethi,[c] Prashant Bankar,[a] Ratna Chauhan*[d] and Suresh W. Gosavi *[aef]

In photocatalytic systems, the efficient generation, separation, and transport of photoinduced charge carriers are essential to achieving high-performance hydrogen production. Semiconductor composites offer a promising route to enhance these processes by leveraging differences in energy band alignments to facilitate charge separation. In this study, ZnO/Al_2O_3 and $ZnO/Al_2O_3/CuO$ nanocomposites were synthesized *via* a facile one-step hydrothermal method. Comprehensive structural and surface analyses using X-ray diffraction (XRD), Raman spectroscopy, filed emission scanning electron microscopy (FESEM), high resolution transmission electron microscopy (HRTEM), Brunauer–Emmett–Teller (BET), X-ray photoelectron spectroscopy (XPS), and ultraviolet photoelectron spectroscopy (UPS) confirmed the successful formation and heterojunction interface of the composites. UV-Vis diffuse reflectance spectroscopy revealed a significant bandgap narrowing, with values of ~2.94 eV for ZnO/Al_2O_3 and ~2.19 eV for $ZnO/Al_2O_3/CuO$—both lower than that of pristine ZnO—indicating improved visible-light absorption. Theoretical band structure calculations further supported the experimental findings and confirmed the energetic favorability for interfacial charge transfer. UPS measurements were employed to determine the work function, revealing efficient band alignment among the constituent semiconductors, thereby promoting effective charge separation and transport. Photocatalytic hydrogen evolution experiments demonstrated superior activity for the ternary composite, with hydrogen generation rates of 676.85 μmol h^{-1} g^{-1} (ZnO), 1448.62 μmol h^{-1} g^{-1} (ZnO/Al_2O_3), and 1888.66 μmol h^{-1} g^{-1} ($ZnO/Al_2O_3/CuO$), highlighting the interfacial charge transfer enhancement driven by heterojunction formation and bandgap engineering. These results indicate that the $ZnO/Al_2O_3/CuO$ nanocomposite is a highly promising photocatalyst for efficient solar-driven hydrogen production.

Received 7th July 2025,
Accepted 19th November 2025

DOI: 10.1039/d5ya00191a

rsc.li/energy-advances

1. Introduction

Hydrogen is recognized as a clean, renewable, and high-energy-density fuel, making it a promising alternative to fossil fuels for sustainable energy applications.[1] Its utilization produces only water as a byproduct, rendering it environmentally benign. The growing global demand for clean energy has intensified research into efficient and economical hydrogen production technologies. Among various methods, photocatalytic water splitting using semiconductor materials has emerged as an environmentally friendly and sustainable route, as it harnesses solar energy to generate hydrogen directly from water without carbon emissions.[2] The efficiency of this process, however, strongly depends on the properties of the photocatalyst, including its band structure, charge separation efficiency, and light absorption capability. Photocatalysis offers several benefits, such as the direct utilization of abundant solar energy, mild operating conditions, and the capability to integrate energy conversion and storage processes. Nevertheless, single-component photocatalysts often exhibit inherent limitations that restrict their efficiency. Therefore, developing composite photocatalysts that combine materials with complementary properties has become a crucial strategy to overcome these challenges and enhance overall photocatalytic performance.

[a] *Center for Advanced Studies in Material Science and Solid-State Physics, Department of Physics, Savitribai Phule Pune University (formally Pune University), Pune 411 007, India. E-mail: swg@physics.unipune.ac.in*
[b] *Department of Environmental Science, Savitribai Phule Pune University (Formerly University of Pune), Pune 411007, India*
[c] *Department of Chemistry, C. T. Bora College, Shirur, Pune, 412210, India*
[d] *School of Nano Science, Central University of Gujrat, Kundhela, 391107, Vadodara, India. E-mail: ratna.chauhan@cug.ac.in*
[e] *Photocatalysis International Research Centre, Research Institute for Science & Technology, Tokyo University of Science, 2641 Yamazaki, Noda, Chiba 278-8510, Japan*
[f] *School of Chemistry, University of Melbourne, VIC 3010, Australia*

In this context, the rational design of composite photocatalysts requires careful consideration of several essential parameters, particularly band structure matching, efficient charge transfer pathways, and chemical compatibility among the components. Proper alignment of conduction and valence band edges facilitates effective charge separation and transfer, thereby improving photocatalytic efficiency. By tailoring the electronic structure and interfacial properties of different semiconductors, it is possible to construct heterojunctions that suppress electron–hole recombination and extend the absorption range toward the visible region of the solar spectrum.

Ternary oxide composites with nanoscopic features have recently gained significant attention due to their synergistic properties and multifunctional capabilities, leading to applications in catalysis,[3] controlled doping, sensing, and filtration.[4–6] Among these, the combination of copper oxide (CuO), zinc oxide (ZnO), and aluminum oxide (Al_2O_3) has been particularly appealing because of the distinct yet complementary characteristics of the individual components.[7,8] Despite their potential, only a limited number of studies have reported the successful synthesis of ZnO/Al_2O_3/CuO nanocomposites through unified approaches.[9,10] These materials have demonstrated potential in photocatalytic degradation of pollutants,[11,12] CO_2 reduction,[13–16] photoelectrochemical (PEC) water splitting for hydrogen generation,[9,17] and water oxidation,[18] underscoring their versatility and practical significance.[19]

Individually, each oxide exhibits unique advantages and inherent limitations. CuO, a p-type semiconductor with a narrow bandgap (1.2–1.9 eV), shows strong visible-light absorption and good catalytic properties but suffers from high electron–hole recombination and stability issues.[20,21] ZnO, an n-type semiconductor with a wide bandgap ($\sim$3.2 eV), offers high quantum yield, environmental benignity, and excellent oxidative capability but is limited by poor visible-light response.[22,23] Al_2O_3, known for its chemical and thermal stability, provides structural robustness but lacks photoactivity and electrical conductivity.[24]

Integrating these oxides into a ternary ZnO/Al_2O_3/CuO composite combines their complementary attributes.[25] ZnO provides a stable photoactive base, CuO enhances visible-light absorption and acts as a charge separation center due to its p-type conductivity, while Al_2O_3 improves surface area, dispersion, and stability. The band alignment between ZnO allows efficient charge transfer, where photogenerated electrons move from CuO to ZnO and holes migrate in the opposite direction, thereby minimizing recombination losses. Al_2O_3 further assists by preventing particle agglomeration and providing additional active sites. Such band structure matching and interfacial synergy make ZnO/Al_2O_3/CuO a suitable composite for photocatalytic hydrogen production.

Various synthesis techniques such as sol–gel,[26] hydrothermal,[27] sonochemical,[28] microwave-assisted combustion,[29,30] and co-precipitation[27] have been employed to prepare nanocomposites with tunable physicochemical properties. Among these, the hydrothermal method is particularly advantageous due to its simplicity, cost-effectiveness, and ability to yield highly homogeneous and crystalline materials under mild conditions. The control of temperature, precursor concentration, and reaction time directly influences the crystal structure, morphology, surface area, and optical properties, thereby tuning the photocatalytic efficiency of the final composite.[31–33]

In the present study, ZnO, ZnO/Al_2O_3, and ZnO/Al_2O_3/CuO nanocomposites were synthesized *via* the hydrothermal route and systematically characterized by X-ray diffraction (XRD), ultraviolet-visible (UV-Vis) spectroscopy, field emission scanning electron microscopy (FESEM), high-resolution transmission electron microscopy (HRTEM), energy-dispersive X-ray spectroscopy (EDS), Brunauer–Emmett–Teller (BET) surface area analysis, and X-ray photoelectron spectroscopy (XPS). The electronic structure was examined by ultraviolet photoelectron spectroscopy (UPS) to elucidate band alignment. The photocatalytic activity of the prepared materials was evaluated for hydrogen evolution under UV light irradiation. The enhanced photocatalytic performance of the ternary ZnO/Al_2O_3/CuO nanocomposite is attributed to its optimized band structure, efficient charge separation, and improved surface characteristics. The novelty of this work lies in the strategic design and synthesis of a ternary oxide heterostructure with tailored interfacial properties to achieve superior photocatalytic hydrogen production efficiency.

2. Experimental

2.1 Materials

Aluminium nitrate nonahydrate, ($Al(NO_3)_3{\cdot}9H_2O$), zinc chloride ($ZnCl_2$), copper nitrate trihydrate ($Cu(NO_3)_2{\cdot}3H_2O$), urea ($CO(NH_2)_2$), and oxalic acid ($COOH{\cdot}2H_2O$) all are analytical grade chemicals used in the present work. Distilled water and ethanol were used without additional purifications.

2.2 Synthesis of ZnO, ZnO/Al_2O_3 and ZnO/Al_2O_3/CuO nanocomposite

2.2.1 Synthesis of ZnO nanosheets. ZnO nanosheets were synthesized *via* a facile single-step hydrothermal route. In a typical synthesis, 0.1 M zinc chloride ($ZnCl_2$), 0.6 M urea ($CO(NH_2)_2$), and 0.1 M oxalic acid dihydrate ($COOH{\cdot}2H_2O$) were dissolved in 100 mL of distilled water under constant magnetic stirring at room temperature for 30 minutes. The resulting homogeneous solution was transferred into a Teflon-lined stainless-steel autoclave and heated at 140 °C for 14 hours. After naturally cooling to room temperature, the precipitate was collected, washed thoroughly with distilled water and ethanol to remove any residual impurities, and dried at 70 °C for 12 hours. The dried powder was then calcined at 450 °C for 4 hours to obtain crystalline ZnO nanosheets.

2.2.2 Synthesis of ZnO/Al_2O_3 nanocomposite. The ZnO/Al_2O_3 nanocomposite was synthesized using the same hydrothermal method described above, with the inclusion of 0.1 M aluminum nitrate nonahydrate ($Al(NO_3)_3{\cdot}9H_2O$) into the precursor solution. The mixture was stirred and treated hydrothermally under identical conditions (140 °C for 14 hours),

followed by cooling, washing, and drying at 70 °C. The resulting powder was calcined at 450 °C for 4 hours to ensure complete crystallization and oxide phase formation.

2.2.3 Synthesis of ZnO/Al_2O_3/CuO nanocomposite. For the synthesis of the ternary ZnO/Al_2O_3/CuO nanocomposite, 0.1 M of both aluminum nitrate nonahydrate ($Al(NO_3)_3{\cdot}9H_2O$) and copper nitrate trihydrate ($Cu(NO_3)_2{\cdot}3H_2O$) were simultaneously added to the original ZnO precursor solution. The synthesis procedure including stirring, hydrothermal treatment at 140 °C for 14 hours, and subsequent cooling, washing, and drying was identical to the previous steps. Finally, the dried sample was calcined at 450 °C for 4 hours to yield the ZnO/Al_2O_3/CuO nanocomposite.

2.3 Photocatalytic hydrogen generation by water splitting

Photocatalytic hydrogen evolution experiments were conducted in a closed batch quartz reactor system to evaluate the hydrogen production efficiency of ZnO, ZnO/Al_2O_3, and ZnO/Al_2O_3/CuO nanocomposites under UV light irradiation. A 125 W mercury vapor UV lamp served as the irradiation source, positioned horizontally at a fixed distance of approximately 10 cm from the surface of the reaction mixture to ensure uniform UV exposure while minimizing thermal effects. The entire reactor setup was enclosed within a reflective aluminum housing to enhance light utilization by evenly distributing the incident radiation across the reaction surface. For each experiment, 20 mg of photocatalyst was dispersed in a reaction mixture containing 25 mL of deionized water and 5 mL of methanol, which acted as a sacrificial electron donor. Platinum (0.5 wt%) was preloaded onto the photocatalyst as a co-catalyst to promote hydrogen evolution. The reactor, a 100 mL quartz vessel sealed with a gas-tight septum, was purged with high-purity nitrogen gas for 20 minutes prior to irradiation to eliminate dissolved oxygen and other gaseous impurities. Continuous magnetic stirring was maintained to ensure a homogeneous suspension during the reaction. The system was water-cooled to maintain a constant reaction temperature of 25 ± 2 °C and to prevent overheating of both the reactor and the photocatalyst suspension. The photocatalytic reaction was initiated under UV irradiation, and evolved gases were periodically sampled (0.5 mL) through the septum using a gas-tight syringe. The hydrogen content in the gas phase was quantified using a Shimadzu gas chromatograph equipped with a 5 Å molecular sieve column and a thermal conductivity detector (TCD), with calibration performed using a pre-established standard curve.

2.4 Physico-chemical characterization

UV-visible absorbance spectra for the samples were recorded on JASCO V-670 spectrophotometer. X-Ray diffraction (XRD) technique was used to analyze crystal structure of the samples. The X-ray diffraction pattern was recorded using Bruker D8-Advanced Diffractometer in the 2θ range of 20–80 degrees which were operated at 40 kV and 30 mA. Field emission scanning electron microscopy (FESEM) analysis was carried out on Hitachi S-4800 instrument. Samples were prepared with drop casting on silicon substrate, which was coated with thin platinum layer. Transmission electron microscopy (TEM) analysis was carried out on JEM 2200FS JEOL. Brunauer–Emmett–Teller (BET) technique (Quantachrome Instruments v3.01) was used to find the surface area using N_2 physisorption technique. Molecular vibrations and structural characteristics were studied using Raman spectroscopy model: thermo scientific spectrometer (excitation wavelength = 532 nm). X-ray photoelectron spectroscopy (XPS) and Ultraviolet photoelectron spectroscopy (UPS) analysis was carried out using ESCA-3000, VG Scientific to observe binding energies. Fluorescence spectra were recorded using the photo-luminescence (PL) spectrophotometer (Model: Fluorolog, HORIBAJOBINYVON).

3. Result and discussion

3.1 UV-visible spectra

The optical properties of the synthesized ZnO, ZnO/Al_2O_3, and ZnO/Al_2O_3/CuO nanocomposites were investigated using UV-Visible diffuse reflectance spectroscopy (UV-Vis DRS). As shown in Fig. 1(a), the pure ZnO exhibited a strong absorption peak at 352 nm, characteristic of its band-to-band electronic transition in the UV region. The ZnO/Al_2O_3 nanocomposite showed a slight blue shift, with an absorption peak at 340 nm, indicating possible quantum confinement or interface effects due to Al_2O_3 incorporation. For the ZnO/Al_2O_3/CuO nanocomposite, three

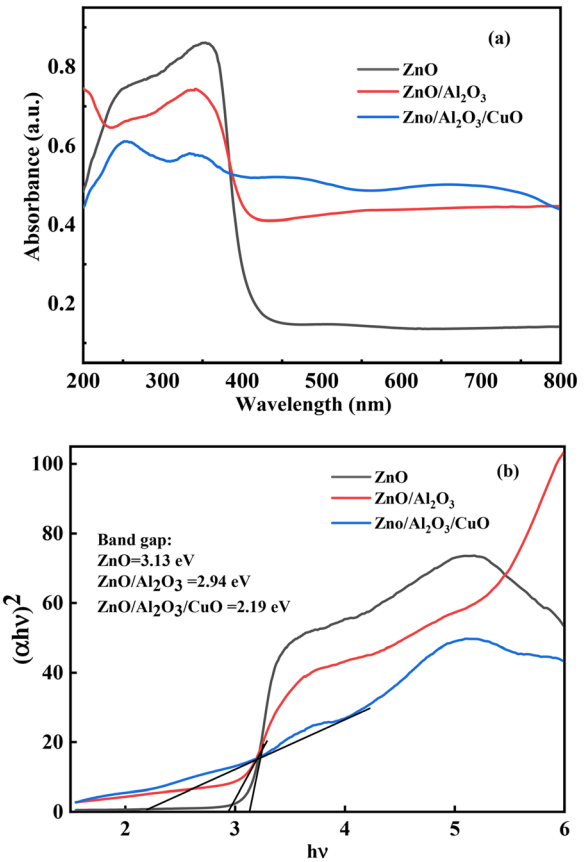

Fig. 1 (a) UV-Visible spectra and (b) Tauc plot of ZnO, ZnO/Al_2O_3 and ZnO/Al_2O_3/CuO nanocomposite.

distinct absorption peaks were observed at 254 nm, 336 nm, and 452 nm. The peak at 254 nm is attributed to high-energy transitions in the ZnO matrix, while the absorption edge at 452 nm corresponds to CuO incorporation, enabling enhanced visible-light absorption. These shifts in absorption behaviour reflect modifications in the electronic structure and band alignment among the constituent semiconductors.

The absorption features are directly associated with electronic transitions from the valence band (VB) to the conduction band (CB), which define the material's optical band gap (E_g). The band gap energy was calculated using the Tauc method, which is based on the Wood and Tauc equation:

$$(\alpha h\nu)^n = A(h\nu - E_g) \quad (1)$$

In this equation, 'α' represents the absorption coefficient, 'h' is Planck's constant, 'ν' is the frequency, 'E_g' is the band gap energy, A is constant, and 'n' depends on the type of electronic transition: (n = 1/2) for direct allowed transitions and n = 2 for indirect allowed transitions.[32]

Fig. 1(b) shows the E_g value for ZnO, ZnO/Al_2O_3 and ZnO/Al_2O_3/CuO nanocomposite is 3.13 eV, 2.94 eV and 2.19 eV respectively. The results suggest a synergistic interaction among ZnO, CuO, and Al_2O_3 metal oxides. The E_g value for all the three synthesized samples lies in the UV-visible region. This means that all three photocatalysts have enhanced photocatalytic activity under UV light.

3.2 X-ray diffraction

The XRD patterns of synthesized ZnO/Al_2O_3/CuO nanocomposite, ZnO/Al_2O_3 nanocomposite and ZnO nanoparticles are shown in Fig. 2(a)–(c). In ZnO X-ray diffraction pattern, the characteristic diffraction appears at 31.74°, 34.35°, 36.25°, 47.48°, 56.60°, 62.81°, 66.42°, 67.92°, 69.13°, 72.43°, 76.94° correspond to the planes (100), (002), (101), (102), (110), (103), (200), (112), (201), (004) and (202) respectively Fig. 2(b), confirm the hexagonal structure of ZnO (JCPDS: 01-076-0704). The X-rays diffraction studies confirmed wurtzite phase and all diffraction peak agreed with the reported JCPDS data. No any other peak observed confirm the purity of sample. The characteristic diffraction peaks appeared at 2θ values 32.3°, 35.35°, 38.16° and 48.5° corresponding to plane (002), ($\bar{1}$11), (111) or (200) and ($\bar{2}$02) for the CuO respectively (Fig. 2(b)). As expected, the XRD spectra obtained from ZnO/Al_2O_3/CuO nanocomposite system, Fig. 2(c), is indicating monoclinic crystal structure (JCPDS card no 00–041-0254). In the X-ray diffraction pattern of ZnO/Al_2O_3 and ZnO/Al_2O_3/CuO nanocomposite, peaks indicative for the Al_2O_3 phase are barely visible (weaker diffraction), which suggests that Al_2O_3 crystallites are either highly dispersed or amorphous structure.[31] Here we have calcined all samples at 450 °C, and up to this temperature, alumina remains in amorphous phase.

3.3 FESEM

FESEM and energy dispersive X-ray spectroscopy (EDS) were employed to examine the surface morphology and elemental

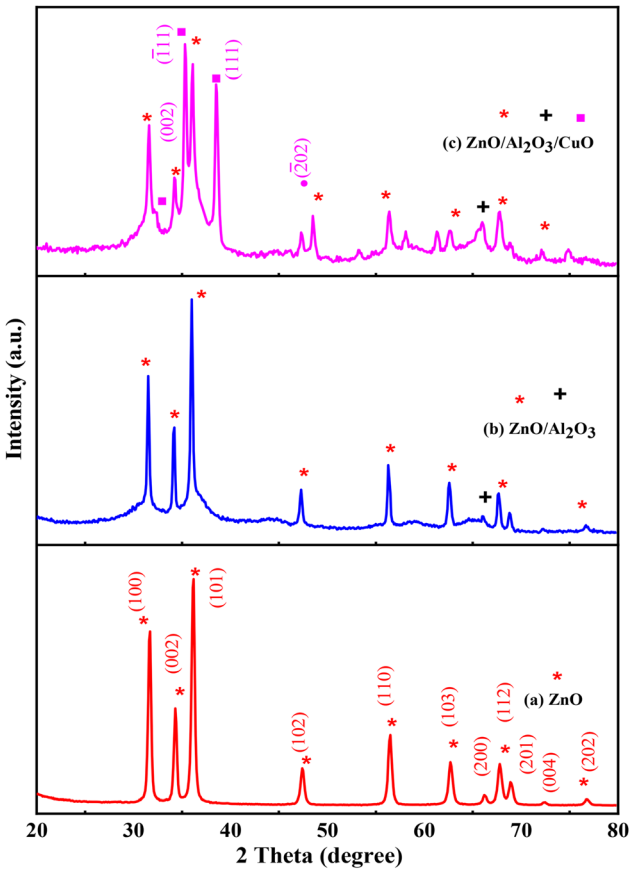

Fig. 2 X-Ray diffraction patterns of (a) ZnO, (b) ZnO/Al_2O_3, and (c) ZnO/Al_2O_3/CuO nanocomposite.

composition of the synthesized nanomaterials. FESEM images of ZnO (Fig. 3(a) and (b)) reveal the formation of multi-layered, ultrathin nanosheets with lateral dimensions ranging from approximately 180 to 450 nm and a thickness of less than 29 nm. These nanosheets exhibit a stacked architecture, contributing to an increased surface area. In the case of the ZnO/Al_2O_3 nanocomposite (Fig. 3(c) and (d)), the morphology displays ZnO nanosheets integrated with distinct spiky flower-like structures characteristic of Al_2O_3. This hybrid structure confirms successful composite formation and suggests a significant enhancement in surface roughness and overall surface area, which is favourable for photocatalytic activity. FESEM images of the ZnO/Al_2O_3/CuO nanocomposite (Fig. 3(e) and (f)) show a heterogeneous microstructure, with visible contrasts in brightness indicating the presence of different phases. The Z-contrast suggests that CuO and ZnO regions appear brighter than Al_2O_3 due to their higher atomic numbers. The CuO nanoparticles are nearly spherical with an average size of ~50 nm, and the overall composite exhibits porous features and interparticle voids, which further enhance the specific surface area. The ZnO/Al_2O_3 nanocomposite exhibits a multi-layered, ultrathin nanosheet morphology that facilitates enhanced mass transport by reducing diffusion resistance and allowing better penetration of light and reactant molecules into the catalyst matrix. In the ZnO/Al_2O_3/CuO nanocomposite,

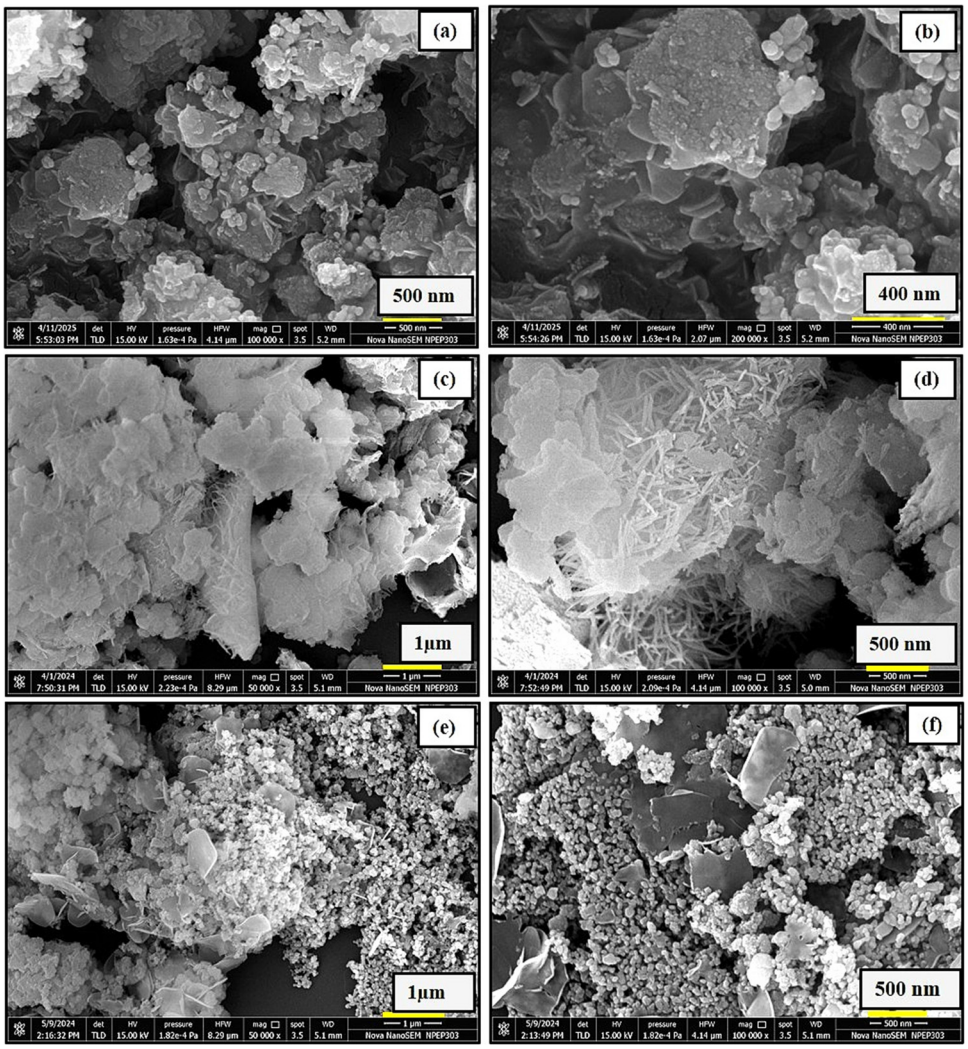

Fig. 3 FESEM Micrograph for ZnO (a), (b), ZnO/Al_2O_3 (c), (d), and $ZnO/Al_2O_3/CuO$ nanocomposite (e), (f).

the uniform dispersion of nanoparticles and well-defined heterojunctions improve charge separation efficiency and increase the density of reactive surface sites. Additionally, the increased surface roughness and curvature enhance the adsorption capacity, promoting stronger interactions between the catalyst surface and target molecules.[34,35] Elemental distribution was analysed using EDS elemental mapping (Fig. 4), which shows a uniform distribution of Zn, Al, Cu, and O elements across the sample surface. The EDS spectrum (Fig. 4(a)) confirms the presence of these elements, validating the successful synthesis of the $ZnO/Al_2O_3/CuO$ ternary nanocomposite.

3.4 HRTEM

Transmission electron microscope analysis confirming the successful formation of synthesized $ZnO/Al_2O_3/CuO$ nanocomposite. The synthesized sample shows spherical shape of CuO nanoparticles, spike like structure of Al_2O_3 and ultrathin nanosheets-like structure of ZnO confirm the presence of all three nanomaterials in nanocomposite. The TEM image (Fig. 5) shows the partial agglomeration trend of ZnO, Al_2O_3 and CuO nanoparticles owing to overloading of Al_2O_3 and hydrothermal conditions, which indicates the formation of ternary nanocomposite. Every nanoparticle is associated with surrounding nanoparticles and no individual ZnO, Al_2O_3 and/or CuO nanoparticles remain, which also confirmed the effective formation of ternary nanocomposite of $ZnO/Al_2O_3/CuO$. The HRTEM image shows the interplanar distance are 0.14 nm, 0.24 nm and 0.25 nm corresponding to the diffraction plane (400), (101) and (220) of ZnO, Al_2O_3 and CuO; which is in closed agreement with d spacing obtained from XRD pattern of ZnO, Al_2O_3 and CuO respectively.

3.5 Raman spectroscopy analysis

Raman spectroscopy was employed to investigate the structural, compositional, and phase characteristics of the synthesized nanostructures, namely pure ZnO, ZnO/Al_2O_3, and $ZnO/Al_2O_3/CuO$ nanocomposites, recorded at room temperature as shown in Fig. 6.

The Raman spectrum of pure ZnO nanosheets exhibits well-defined peaks at approximately 335 cm^{-1}, 438 cm^{-1}, and

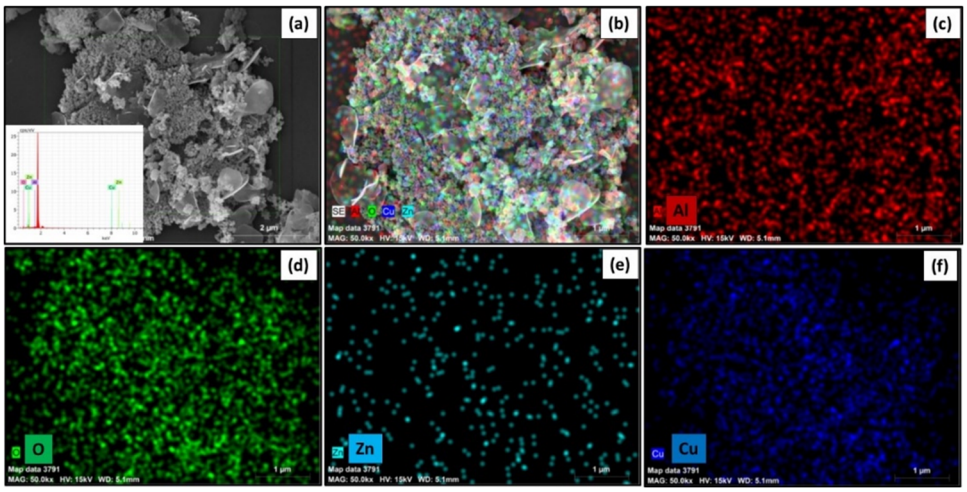

Fig. 4 Elemental mapping of the ZnO/Al_2O_3/CuO nanocomposite: (a) FE-SEM with EDS, (b) overlapped elemental map, (c) Al elemental map, (d) O elemental map, (e) Zn elemental map, and (f) Cu elemental map.

586 cm^{-1}. The peak at 438 cm^{-1} is attributed to the E_2 (high) phonon mode, a characteristic mode of the wurtzite hexagonal ZnO structure, indicating good crystallinity. The 335 cm^{-1} peak corresponds to the difference between E_2 (high) and E_2 (low) modes, suggesting lattice vibration interactions typical of ZnO nanostructures. The 586 cm^{-1} band is commonly associated with the A_1 (LO) or E_1 (LO) mode, often linked to structural defects such as oxygen vacancies or zinc interstitials, indicating slight disorder within the ZnO lattice. Upon incorporation of Al_2O_3 into ZnO (ZnO/Al_2O_3), the spectrum retains the prominent E_2 (high) mode at 436.3 cm^{-1} and the E_2 high–E_2 low mode at 335 cm^{-1}, demonstrating the persistence of the ZnO wurtzite structure even after the formation of the heterostructure. However, the reduced intensity and broadening of peaks suggest possible strain effects or lattice distortion induced by Al_2O_3 incorporation.

The Raman spectrum of the ternary ZnO/Al_2O_3/CuO nanocomposite reveals a more complex vibrational profile with multiple peaks at 314.01 cm^{-1}, 398.8 cm^{-1}, 555 cm^{-1}, 635.6 cm^{-1}, and a broad band centred around 1095 cm^{-1}. The peak at 314.01 cm^{-1} corresponds to the A_g mode of monoclinic CuO, while the 398.8 cm^{-1} peak is attributed to the B_g mode of CuO. The 555 cm^{-1} and 635.6 cm^{-1} bands are typically associated with oxygen-related lattice vibrations in CuO or Al–O bond distortions,

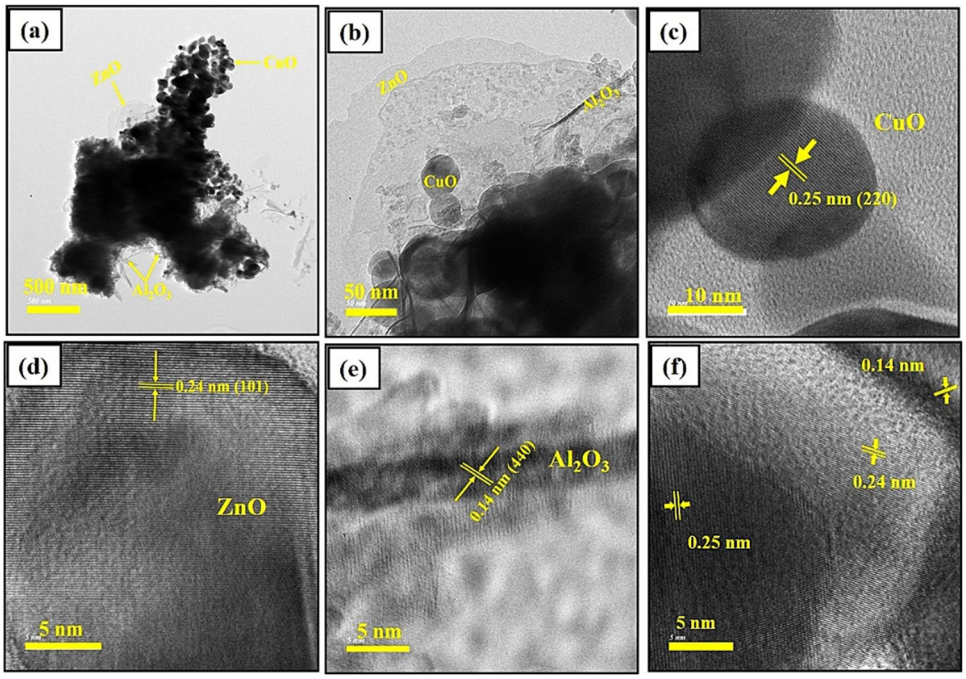

Fig. 5 (a), and (b) TEM images for ZnO/Al_2O_3/CuO nanocomposite, (c)–(f) HRTEM image for CuO, ZnO, Al_2O_3 in nanocomposite respectively.

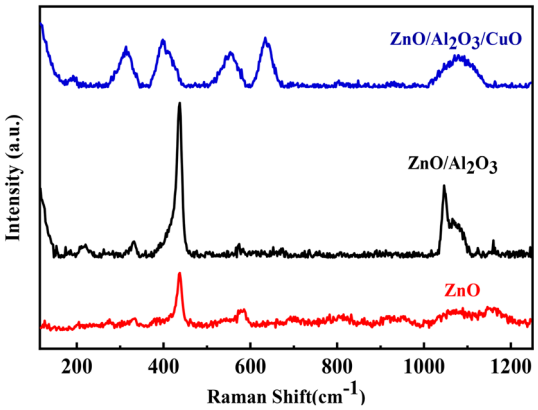

Fig. 6 Raman spectrum of ZnO, ZnO/Al_2O_3 and $ZnO/Al_2O_3/CuO$ nanocomposite.

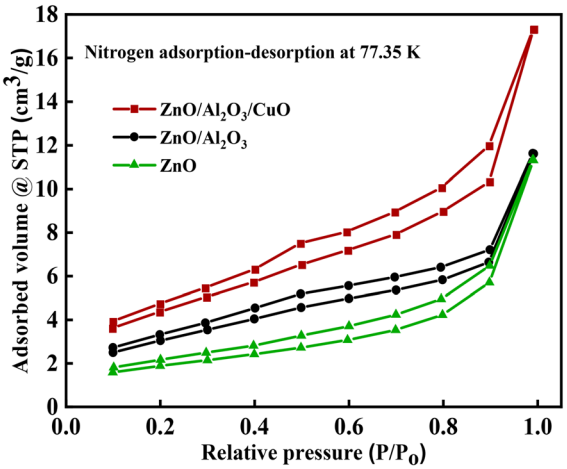

Fig. 7 BET curves of ZnO, ZnO/Al_2O_3, and $ZnO/Al_2O_3/CuO$ nanocomposite.

implying successful integration of CuO and Al_2O_3 phases into the ZnO matrix. The broad peak observed at 1095 cm^{-1} is assigned to multi-phonon scattering associated with the CuO component. This high-wavenumber region is indicative of overtones and combination bands arising due to strong electron–phonon coupling and the disordered nature of the CuO phase within the composite. The presence of such features suggests complex vibrational dynamics, possibly resulting from interfacial interactions and phonon confinement effects in the nanocomposite.

3.6 BET measurement

The surface area plays an important role in hydrogen generation and photocatalytic activity. BET surface area of the synthesized samples ZnO, ZnO/Al_2O_3, and $ZnO/Al_2O_3/CuO$ nanocomposite were recorded under nitrogen adsorption–desorption isotherm at 77.35 K, and the corresponding isotherms plots are shown in Fig. 7. The BET measurements reveal the surface area of ZnO, ZnO/Al_2O_3, and $ZnO/Al_2O_3/CuO$ nanocomposite are 77.763 $m^2\ g^{-1}$, 135.056 $m^2\ g^{-1}$, and 437.075 $m^2\ g^{-1}$ respectively. As observed in BET measurement, the ZnO nanosheets has low surface area, however the surface area increases after formation of ZnO/Al_2O_3 and $ZnO/Al_2O_3/CuO$ nanocomposite. The isotherm of all samples corresponds to the type IV isotherm (IUPAC), indicating the presence of mesoporous materials.[16,33] Therefore, it can play a significant role in hydrogen generation *via* water splitting. BET analysis shows the sample $ZnO/Al_2O_3/CuO$ have high surface area and active catalytic sites may produce significant hydrogen production.

3.6 XPS analysis

Chemical composition of $ZnO/Al_2O_3/CuO$ nanocomposite was determined by XPS analysis. The XPS spectra were calibrated with carbon 1s peak located at 284.6 eV as the reference position. Full survey scan confirmed the existence of Cu, Zn, Al and O elements (Fig. 8(a)). Fig. 8(c) shows peaks assigned to Zn 2p level. Two distinct peaks appeared at 1021.3 eV and 1043.85 eV suggest the presence of Zn^2. The Al 2p fitted spectra in Fig. 8(d) reveal the presence of an oxide peak at a binding energy of 73.7 eV, along with an aluminium metal peak at 71.75 eV. This alignment closely matches the reported peak separation of 2.45 eV.[36] O1s spectra in Fig. 8(b) is deconvoluted into two peaks having binding energy 527 eV and 529.45 eV. The low binding energy is ascribed to O_2^- ions enclosed and composite system. The signal serves as an indicator of quantity of oxygen atoms are completely oxidized. High resolution spectra of Cu 2p (Fig. 8(e)) are deconvoluted into Cu $2p_{3/2}$ and Cu $2p_{1/2}$. The spectrum exhibits two additional peaks positioned at 961.22 eV and 940.5 eV which are related to CuO.[37] These satellite peaks typically arise from the "shake up" phenomenon, where excess electrons are stimulated into higher energy states Cu $2p_{1/2}$ peak at 952.2 eV and Cu $2p_{3/2}$ peak was attributed at 932.35 eV was attributed to Cu^+ and Cu.[38] The high-resolution XPS spectra of the O 1s, Al 2p, and Zn 2p core levels for the $ZnO/Al_2O_3/CuO$ and ZnO/Al_2O_3 nanocomposites are shown in Fig. S1(a)–(f). A noticeable shift in the binding energies of these elements is observed in the $ZnO/Al_2O_3/CuO$ nanocomposite compared to ZnO/Al_2O_3, indicating a change in the electronic environment and strong interfacial interaction among the constituent phases. The observed binding energy shifts are 0.8 eV for O 1s, 0.7 eV for Al 2p, and 1.5 eV for Zn 2p, confirming charge redistribution and modification in the oxidation states of the elements. These variations in binding energy provide clear evidence for interfacial charge transfer and successful formation of the $ZnO/Al_2O_3/CuO$ heterostructure.

3.7 Energy band and UPS analysis

The conduction band (E_{CB}) and valence band (E_{VB}) potentials, for ZnO, Al_2O_3 and CuO in $ZnO/Al_2O_3/CuO$ nanocomposite was calculated using the following known equations:

$$E_{CB} = \chi - E_e + 0.5\ E_g$$

$$E_{VB} = E_{CB} - E_g$$

where χ represents the Mulliken electronegativity of the semiconductors (5.75 eV for ZnO, 5.35 eV for Al_2O_3 and 5.80 eV

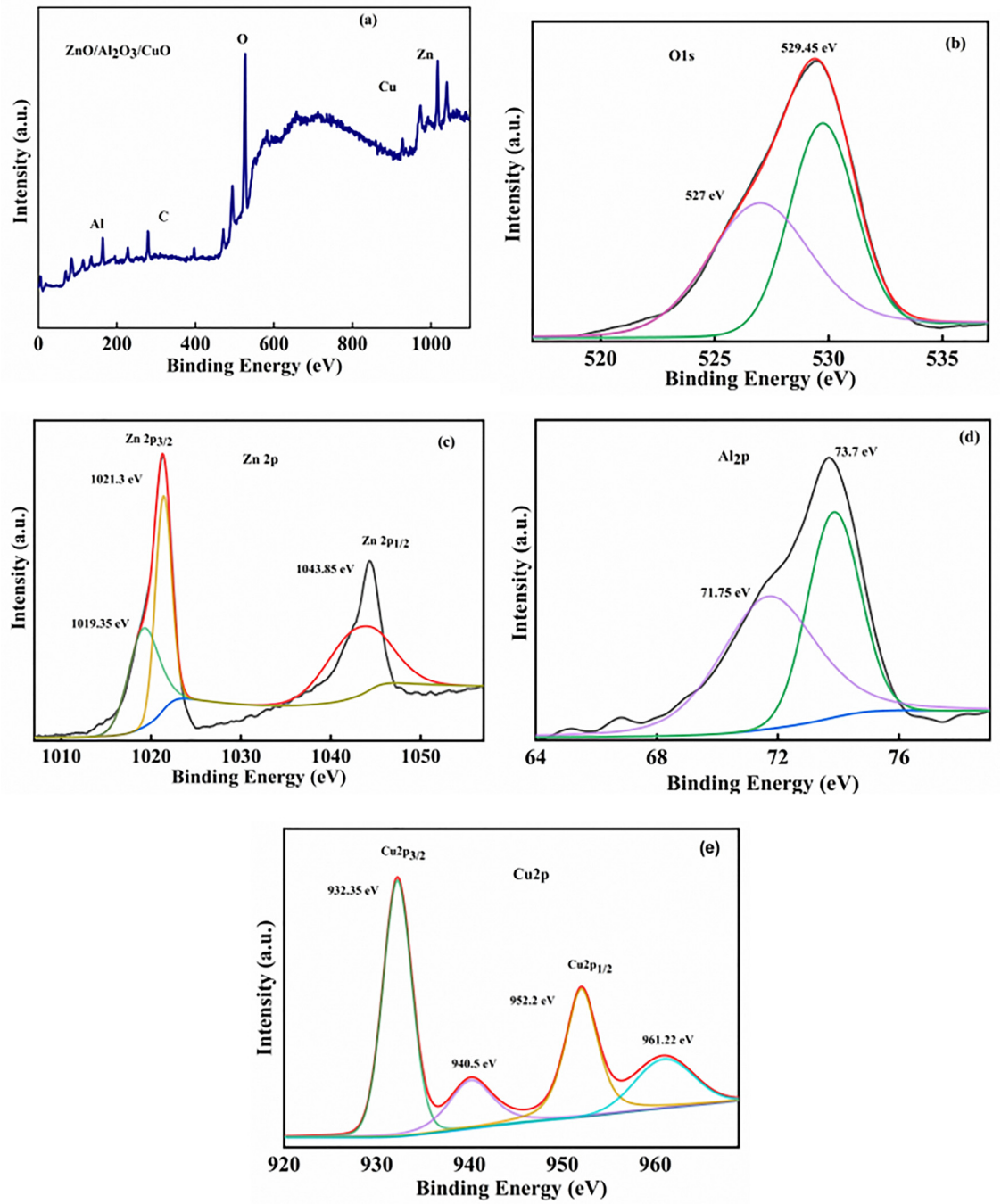

Fig. 8 (a) Survey scan of ZnO/AlO$_3$/CuO nanocomposite, and high resolution XPS spectra of the core level of (b) O1s, (c) Zn 2p, (d) Al 2p and (e) Cu 2p.

for CuO). E_g is the energy gap of the ZnO, Al_2O_3 and CuO is 3.13, 4.4, and 1.4 respectively. E_e is the energy of the free electrons on the hydrogen scale with fixed value 4.5 eV. Thus, the E_{CB} values of ZnO, Al_2O_3 and CuO were −0.31, −1.34, and 0.57 eV, respectively. In the same way, the values of E_{VB} were 2.81, 3.05, and 2.03 eV, respectively. Pure ZnO and ZnO/Al_2O_3 shows low hydrogen evolution (*i.e.* low photocatalytic activity) with respective to ternary composite, it may be larger band gap as in Al_2O_3 and ZnO or small band gap that resulted in higher electron–hole generation recombination rate as in CuO.[39] Fig. 9 shows the schematic illustration of the band gap alignments for ternary composite.

The ultraviolet photoelectron spectroscopy (UPS) spectra of the ZnO/Al_2O_3/CuO nanocomposite on Si substrates are presented in Fig. 10. The results indicate that the onset energy of secondary electrons for the ZnO/Al_2O_3/CuO nanocomposite was estimated to be 15.02 eV, while the Fermi level was determined to be −1.88 eV. When two semiconductors with distinct energy gaps form a heterojunction structure, the energy gaps align at the interface, influencing both the onset

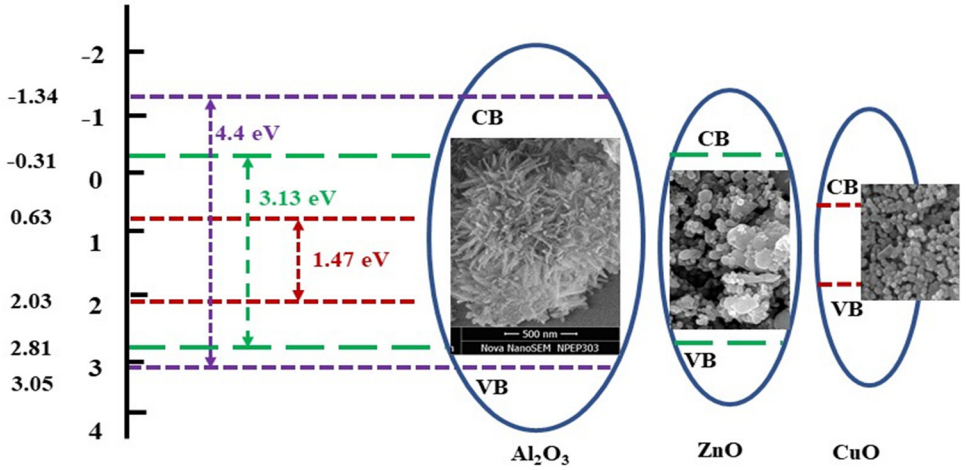

Fig. 9 Schematic diagrams representing energy bands of ZnO/Al_2O_3/CuO nanocomposite.

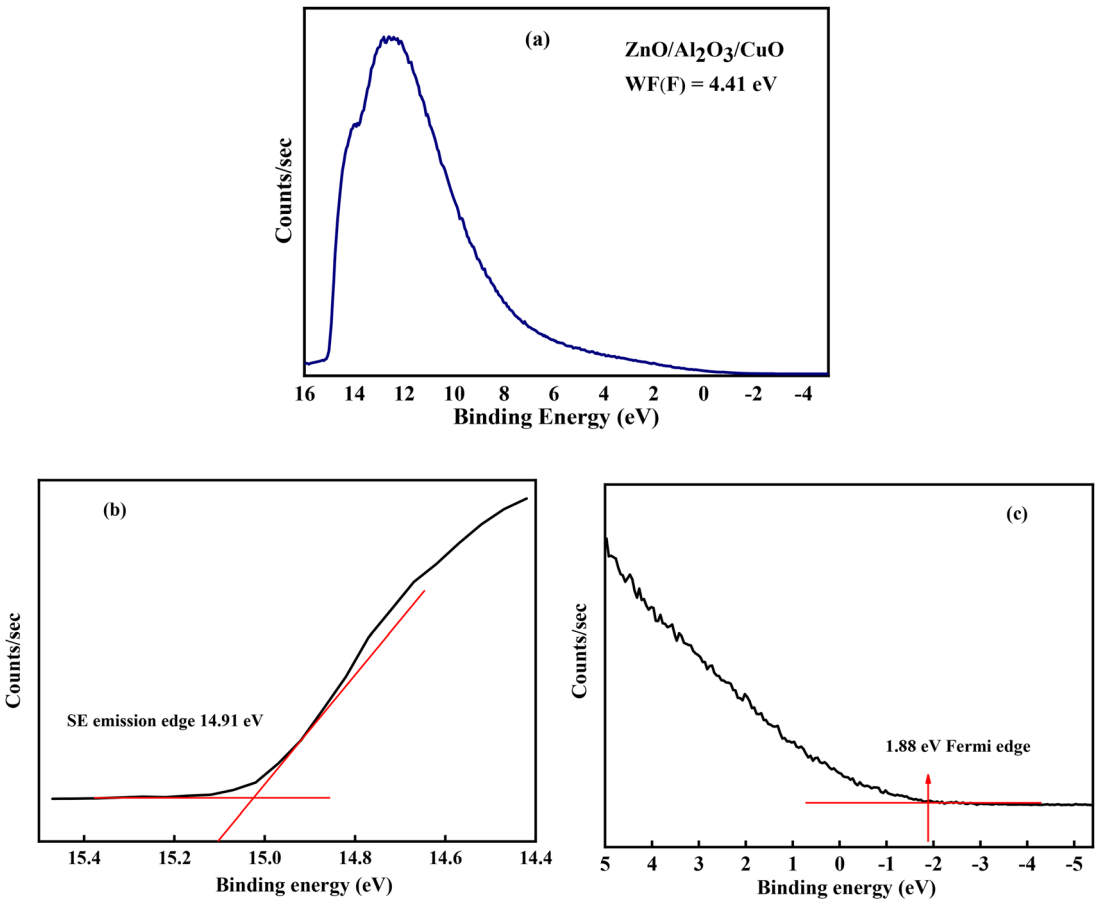

Fig. 10 (a) UPS spectra of the ZnO/Al_2O_3/CuO nanocomposite film showing (b) the secondary edge at high binding energy region related to work function and (c) the low energy region related to valence band maximum.

energy of secondary electrons and the Fermi energy level.[40] Furthermore, the work function (Φ) was calculated using the following equation:

$$\mathrm{WF}\ (\Phi) = h\nu - (E_0 - E_f)$$

where Φ represents the work function, h is Planck's constant, ν is the frequency of UV light, E_0 denotes the onset energy of secondary electrons, and E_f indicates the Fermi level. Based on this equation, the work function of the ZnO/Al_2O_3/CuO nanocomposite was found to be 4.32 eV, which is lower than that of

individual CuO and ZnO nanoparticles.[41,42] A reduced work function implies a higher Fermi level, leading to an increased probability of electron transitions to the conduction band. Additionally, a lower work function also contributes to a higher current density. Consequently, the ZnO/Al_2O_3/CuO nanocomposite system demonstrates enhanced sensitivity compared to ZnO and ZnO/Al_2O_3, supporting the assertion that it exhibits the best H_2 generation performance.

3.8 Photoluminescence and time-resolved photoluminescence analysis

The photoluminescence (PL) and time-resolved photoluminescence (TRPL) spectra of ZnO, ZnO/Al_2O_3, and ZnO/Al_2O_3/CuO nanocomposites are presented in Fig. 11(a) and (b), respectively. The PL spectra were recorded at room temperature with an excitation wavelength of 352 nm. As shown in Fig. 11(a), all samples exhibit a prominent emission peak centered around 458 nm, corresponding to the near-band-edge emission of ZnO nanoparticles. A gradual decrease in PL intensity is observed from pristine ZnO to the ZnO/Al_2O_3/CuO nanocomposite, accompanied by a slight shift in peak position. This reduction in emission intensity indicates suppressed charge carrier recombination, which can be attributed to efficient charge transfer and band bending effects arising from heterojunction formation. In this configuration, the Al_2O_3 layer functions as an insulating barrier that minimizes surface recombination, while the p-type CuO forms a p–n junction with n-type ZnO. This junction promotes spatial separation of photoinduced electrons and holes, thereby enhancing charge transfer efficiency.

The TRPL spectra, shown in Fig. 11(b), further support these findings. The average carrier lifetimes obtained from TRPL fitting are 13.6 ns for pristine ZnO, 15.10 ns for ZnO/Al_2O_3, and 18.78 ns for the ZnO/Al_2O_3/CuO nanocomposite. The significant increase in lifetime for the ternary composite demonstrates more effective suppression of electron–hole recombination due to the synergistic effects of CuO and Al_2O_3. Specifically, the CuO–ZnO heterojunction facilitates charge separation and prolongs carrier lifetime, while Al_2O_3 serves as a passivation layer that reduces surface defects and traps. These results collectively confirm the improved charge carrier dynamics and reduced recombination in the ZnO/Al_2O_3/CuO nanocomposite, which are beneficial for enhancing photocatalytic activity.

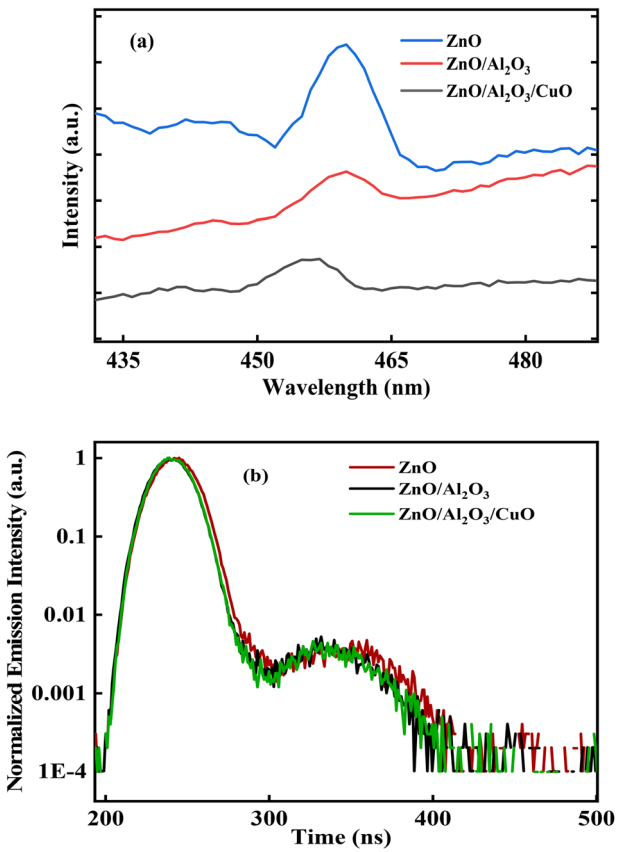

Fig. 11 (a) Photoluminescence (PL) spectra and (b) Time-resolved photoluminescence (TRPL) spectra of ZnO, ZnO/Al_2O_3, and ZnO/Al_2O_3/CuO nanocomposites.

4. Hydrogen generation performance and mechanism

4.1 Photocatalytic hydrogen generation *via* water splitting

The photocatalytic hydrogen generation efficiency of pure ZnO, ZnO/Al_2O_3, and ZnO/Al_2O_3/CuO nanocomposites was systematically investigated *via* water splitting under UV light irradiation, as illustrated in Fig. 12. The comparative H_2 evolution rates for these photocatalysts clearly demonstrate the enhanced activity of the ternary nanocomposite.

The photocatalytic hydrogen generation performance of the synthesized nanomaterials revealed a clear enhancement trend with composite formation. Pristine ZnO nanosheets exhibited a hydrogen evolution rate of 676.85 μmol h^{-1} g^{-1}, primarily due to their inherent semiconducting nature and moderate photon absorption capability in the ultraviolet region. Incorporation of Al_2O_3 into the ZnO matrix significantly improved the H_2

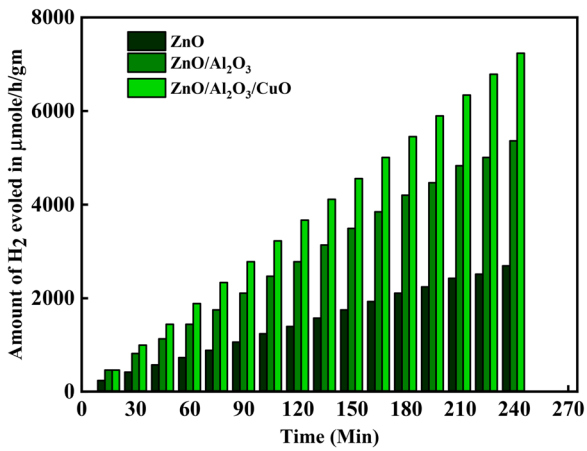

Fig. 12 H_2 evolution rate *via* water splitting using ZnO and ZnO/Al_2O_3 and ZnO/Al_2O_3/CuO nanocomposite.

Table 1 Comparison of structural phase, optical band gap, surface area, and photocatalytic hydrogen evolution performance of ZnO, ZnO/Al_2O_3, and $ZnO/Al_2O_3/CuO$ nanocomposites

Sample	Structural	Optical band gap (eV)	BET surface area ($m^2\ g^{-1}$)	Photocatalytic hydrogen evolution ($\mu mol\ h^{-1}\ g^{-1}$) under UV irradiation	Photocatalytic hydrogen evolution ($\mu mol\ h^{-1}\ g^{-1}$) under visible light irradiation
ZnO	Hexagonal	3.13	77.763	676.85	488.96
ZnO/Al_2O_3	Wurtzite	2.94	135.056	1448.62	962.64
$ZnO/Al_2O_3/CuO$	Monoclinic	2.19	437.075	1888.66	1278.43

production rate to 1448.62 $\mu mol\ h^{-1}\ g^{-1}$. This enhancement can be attributed to the role of Al_2O_3 in suppressing charge carrier recombination, thereby improving the overall photocatalytic efficiency. A further and remarkable improvement was achieved with the ternary $ZnO/Al_2O_3/CuO$ nanocomposite, which demonstrated an outstanding hydrogen evolution rate of 1888.66 $\mu mol\ h^{-1}\ g^{-1}$. The synergistic interaction among ZnO, Al_2O_3, and CuO components contributed to superior light absorption, efficient charge separation, and extended carrier lifetimes, resulting in the highest hydrogen generation performance among all tested samples.

The structural, optical, and catalytic parameters of ZnO, ZnO/Al_2O_3, and $ZnO/Al_2O_3/CuO$ nanocomposites are summarized in Table 1. The results clearly indicate that composite formation leads to a progressive reduction in optical band gap and a significant increase in surface area, both of which contribute to the enhanced photocatalytic hydrogen evolution activity observed for the ternary $ZnO/Al_2O_3/CuO$ system.

Although the $ZnO/Al_2O_3/CuO$ nanocomposite exhibits extended optical absorption into the visible region ($\sim$2.19 eV), the hydrogen evolution rate under visible-light irradiation was found to be significantly lower compared to UV excitation. This behavior arises because visible-light excitation predominantly involves CuO or defect-related states, which generate charge carriers with lower reduction potential and higher electron–hole recombination probability. Moreover, the presence of Al_2O_3 can further restrict interfacial charge transfer under low-energy visible excitation, limiting the effective participation of photoinduced carriers in the hydrogen evolution process. Although the $ZnO/Al_2O_3/CuO$ catalyst exhibits absorption in the visible-light region ($\sim$2.19 eV), photocatalytic H_2 generation under visible light was found to be significantly lower than under UV irradiation (Table 1 and Fig. S2). This reduced activity is attributed to the low-energy excitation of CuO or defect states, which leads to high electron–hole recombination and unfavourable band alignment for proton reduction.[43] Therefore, UV-light-driven experiments are reported to highlight the optimal H_2 generation performance of the catalyst.

4.2 Plausible photocatalytic mechanism

The superior photocatalytic activity of the $ZnO/Al_2O_3/CuO$ nanocomposite can be ascribed to the synergistic interplay between its constituent components and the efficient separation and utilization of photogenerated charge carriers. The proposed mechanism is explained as follows:

1. **Photon absorption and charge generation.** Upon UV light irradiation, ZnO and CuO components absorb photons with energy equal to or greater than their bandgaps, resulting in the excitation of electrons from the valence band (VB) to the conduction band (CB), thereby creating electron–hole (e^-/h^+) pairs:

$$ZnO + h\nu \rightarrow e^-CB_{ZnO} + h^+VB_{ZnO}$$

$$CuO + h\nu \rightarrow e^-CB_{CuO} + h^+VB_{CuO}$$

2. **Charge transfer *via* Z-scheme pathway.** In this ternary system, a direct Z-scheme heterojunction is formed between ZnO and CuO with Al_2O_3 acting as an insulating barrier and charge mediator: the photogenerated electron in the CB of CuO recombines with the hole in the VB of ZnO at the interface. This recombination preserves the strongly reducing electrons in the CB of ZnO and the strongly oxidizing holes in the VB of CuO, which are energetically favourable for redox reactions (Fig. 13).

Recombination step:

$$e^-CB_{CuO} + h^+VB_{ZnO} \rightarrow \text{Heat (non-productive recombination)}$$

As a result, only the electrons in CB of ZnO and holes in VB of CuO participate in surface reactions, achieving efficient spatial charge separation and minimizing recombination losses.

Although Al_2O_3 is not photoactive, it plays a crucial role in the $ZnO/Al_2O_3/CuO$ nanocomposite by regulating interfacial

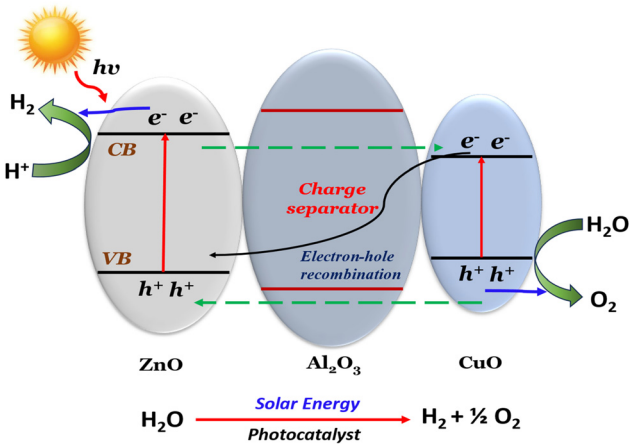

Fig. 13 Plausible Z-scheme photocatalytic mechanism illustrating charge transfer in the $ZnO/Al_2O_3/CuO$ heterojunction for simultaneous hydrogen and oxygen evolution under solar irradiation.

charge dynamics. It physically separates ZnO and CuO, thereby minimizing direct electron–hole recombination at the interface. Its high surface area and thermal stability contribute to the structural integrity and durability of the composite. Additionally, the dielectric nature of Al_2O_3 aids in facilitating interfacial charge transfer by promoting spatial charge separation, ultimately enhancing the overall photocatalytic efficiency.

3. **Surface reactions for water splitting.** Once the charge carriers reach the surface of the nanocomposite, redox reactions are initiated:

At the conduction band (CB) of ZnO, electrons reduce protons (H^+) to generate molecular hydrogen:

$$2H^+ + 2e^- \rightarrow H_2\uparrow$$

At the valence band (VB) of CuO, holes oxidize water molecules to form oxygen and release protons:

$$2H_2O + 4h^+ \rightarrow O_2\uparrow + 4H^+$$

The proposed Z-scheme charge transfer is supported by our experimental analyses. XPS shows binding energy shifts of Zn, O, and Al in the composite, indicating interfacial charge transfer. PL and TRPL results demonstrate suppressed recombination and prolonged carrier lifetimes, while theoretical energy band gap calculation and UPS confirms favourable band alignment and reduced work function. Collectively, these observations provide strong evidence that the photogenerated electrons in CuO recombine with holes in ZnO at the interface, leaving highly reducing electrons in ZnO and strongly oxidizing holes in CuO, consistent with a direct Z-scheme pathway. The Z-scheme photocatalytic architecture offers several mechanistic advantages that significantly enhance the overall efficiency of the $ZnO/Al_2O_3/CuO$ nanocomposite system for hydrogen generation. Unlike traditional type-II heterojunctions, which often compromise the redox potential of charge carriers, the Z-scheme preserves the strong reducing power of the electrons in the conduction band (CB) of ZnO and the strong oxidizing ability of the holes in the valence band (VB) of CuO. This is achieved by the strategic recombination of photogenerated electrons in the CB of CuO with holes in the VB of ZnO at the interface, leaving behind the energetically favorable charge carriers at the respective ends of the band structure. This spatial and energetic separation of charges effectively suppresses bulk and surface recombination losses, thus improving charge carrier lifetime. The presence of Al_2O_3 further enhances this effect by acting as an insulating spacer and charge mediator that physically separates the semiconductors, thereby minimizing direct recombination while facilitating interfacial charge mobility. Additionally, Al_2O_3 contributes to increasing the surface area and structural integrity of the nanocomposite, which benefits catalytic activity. The synergistic interaction among ZnO, Al_2O_3, and CuO leads to enhanced light harvesting, more efficient charge separation, and improved reaction kinetics, resulting in a $\sim$2.8-fold increase in hydrogen evolution rate compared to pristine ZnO.

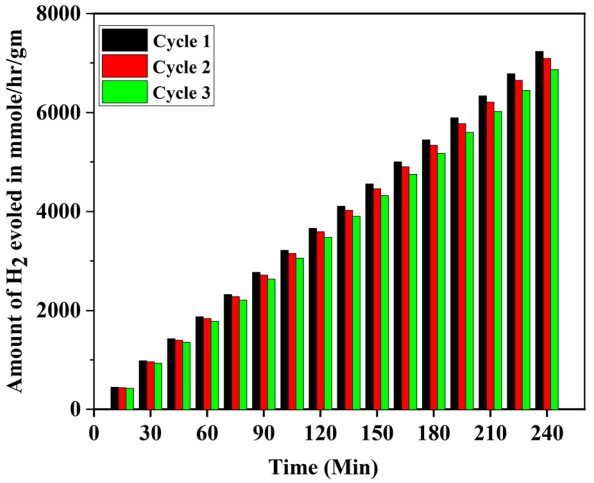

Fig. 14 Photocatalytic hydrogen evolution stability of the $ZnO/Al_2O_3/CuO$ nanocomposite over three consecutive cycles under identical reaction conditions.

4.3 Photocatalytic stability and reusability

The long-term stability and reusability of the $ZnO/Al_2O_3/CuO$ nanocomposite photocatalyst were evaluated through three consecutive photocatalytic hydrogen evolution cycles under identical experimental conditions. After each cycle, the photocatalyst was recovered by centrifugation, thoroughly washed with deionized water and ethanol to remove residual reactants, and then dried before reuse. As presented in Fig. 14, the $ZnO/Al_2O_3/CuO$ nanocomposite demonstrated excellent stability with only a slight decrease in hydrogen evolution rate over successive runs. The initial H_2 generation rate of 1888.5 μmol h^{-1} g^{-1} in the first cycle decreased marginally to 1837.5 μmol h^{-1} g^{-1} and 1781.5 μmol h^{-1} g^{-1} in the second and third cycles, respectively. This minor decline ($\sim$5.7% after three cycles) can be attributed to the possible partial surface adsorption of reaction intermediates or minor photo-corrosion of the active sites during prolonged UV exposure.

The observed results confirm that the $ZnO/Al_2O_3/CuO$ nanocomposite maintains high photocatalytic durability and structural integrity throughout repeated use. The excellent stability performance highlights the strong interfacial coupling between ZnO, Al_2O_3, and CuO components, which effectively prevents structural degradation and maintains efficient charge transfer pathways during the photocatalytic process.

5. Conclusion

This study demonstrates the successful, cost-effective synthesis of a $ZnO/Al_2O_3/CuO$ nanocomposite and its superior photocatalytic performance for hydrogen generation *via* water splitting. The ternary composite exhibited a significantly enhanced hydrogen evolution rate of 1888.66 μmol h^{-1} g^{-1}, compared to 676.85 μmol h^{-1} g^{-1} for pure ZnO and 1448.62 μmol h^{-1} g^{-1} for the ZnO/Al_2O_3 system. The BET surface area increased

markedly from 77.763 $m^2 g^{-1}$ (ZnO) to 135.056 $m^2 g^{-1}$ (ZnO/Al_2O_3) and 437.075 $m^2 g^{-1}$ ($ZnO/Al_2O_3/CuO$), facilitating greater active site availability for photocatalysis. UV-Vis DRS analysis revealed progressive shifts in absorption peaks, including an extended absorption edge at 452 nm for $ZnO/Al_2O_3/CuO$ nanocomposite, indicating improved visible-light harvesting due to CuO incorporation and modified band alignment. HRTEM images and XRD patterns confirmed the effective formation of the ternary nanocomposite, with interplanar spacings of 0.14 nm (ZnO), 0.24 nm (Al_2O_3), and 0.25 nm (CuO) matching their respective diffraction planes. This work establishes a comprehensive framework for engineering multifunctional photocatalysts, integrating structural stability, enhanced charge separation, and broad-spectrum light absorption, paving the way for scalable, efficient, and economically viable solar-to-hydrogen energy conversion technologies.

Author contributions

The contributions of the authors to this work are as follows: Dr Krishna D. Daware was responsible for the methodology, investigation, data analysis, formal analysis, and writing of the original draft. Ms Mayuri Khade contributed to experimental work, data analysis, and formal analysis. Ms Sonali Mhaske, Dr Yogesh Sethi and Mr Prashant Bankar carried out the investigation and formal analysis. Dr Ratna Chauhan and Dr Suresh Gosavi supported the study through conceptual framework, investigation, supervised the research, data curation, editing of the manuscript and writing – review.

Conflicts of interest

The authors declared that there is no conflict of interest.

Data availability

All data generated or analyzed during this study are included in this published article and its supplementary information.

Supplementary information (SI) is available. See DOI: https://doi.org/10.1039/d5ya00191a.

Acknowledgements

SWG and KDD would like to thank to Department of Science and Technology, Government of India for financial support under the Nano Mission project with project no. DST/NM/NT/2021/02-1C-SPPU.

References

1 A. Dehghani, M. Ranjbar and A. Eliassi, Modification of Cu/Zn/Al_2O_3 Catalyst by Activated Carbon Based Metal Organic Frameworks as Precursor for Hydrogen, *J. Inorg. Organomet. Polym. Mater.*, 2018, **28**, 585–593, DOI: 10.1007/s10904-017-0678-6.

2 I. Ahmad, M. Q. Alfaifi, S. Ben Ahmed, M. M. Abduljawad, Y. A. Alassmy, S. A. Alshuhri and T. L. Tamang, Strategies for optimizing sunlight conversion in semiconductor photocatalysts: A review of experimental and theoretical insights, *Int. J. Hydrogen Energy*, 2024, **96**, 1006–1066, DOI: 10.1016/j.ijhydene.2024.11.388.

3 S. M. Botsa, Reduced graphene oxide-assisted TiO_2–Fe_2O_3 ternary nanocomposite for efficient visible-light driven photocatalysis of nitrobenzene and dye pollutants, *Adv. Compos. Hybrid Mater.*, 2025, **8**, 384, DOI: 10.1007/s42114-025-01431-w.

4 N. Alebachew, T. B. Demissie, H. C. A. Murthy, B. A. Gonfa, K. G. von Eschwege, E. Coetsee, E. H. G. Langner, Jayadev and B. H. Doreswamy, Synthesis, characterization, and application of ternary CuO/ZrO_2@S-doped g-C_3N_4 hybrid nanocomposites, *RSC Adv.*, 2025, **15**, 6441–6456, DOI: 10.1039/d4ra08941c.

5 J. Albadi, M. Jalali and H. A. Samimi, Preparation and Characterization of an Efficient Nano-Inorganic Composite of CuO/ZnO/Al_2O_3 for the Catalytic Amination of Aryl Halides in Aqueous Conditions, *Catal. Lett.*, 2018, **148**, 3750–3756, DOI: 10.1007/s10562-018-2567-1.

6 P. Choudhury, S. Ghosh, K. Biswas and B. Basu, A suitably fabricated ternary nanocomposite (Cu–CuO@rGO–SiO_2) as a sustainable and common heterogeneous catalyst for C–S, C–O and C–N coupling reactions, *Nanoscale*, 2024, **16**, 11592–11603, DOI: 10.1039/d4nr01116c.

7 W. Wu, K. Xie, D. Sun, X. Li and F. Fang, CuO/ZnO/Al_2O_3 Catalyst Prepared by Mechanical-Force-Driven Solid-State Ion Exchange and Its Excellent Catalytic Activity under Internal Cooling Condition, *Ind. Eng. Chem. Res.*, 2017, **56**, 8216–8223, DOI: 10.1021/acs.iecr.7b01464.

8 N. Quynh, N. Trang and C. T. Thuy, Synthesis of Composites ZnO–Al_2O_3, ZnO–Al_2O_3–CuO and Evaluation of its Activity for COS Conversion, H_2S Sorption Treatment, *Int. J. Chem. Sci.*, 2017, **15**(4), 210.

9 T. T. N. Hoang, Y. S. Lin, T. N. H. Le, T. K. Le, T. K. X. Huynh and D. H. Tsai, Optimal mixing method of $ZnZrO_x$ and MOR-type zeolite to prepare a bifunctional catalyst for CO_2 hydrogenation to lower olefins, *Adv. Powder Technol.*, 2021, **32**, 1785–1792, DOI: 10.1016/j.apt.2023.104174.

10 N. H. Berahim, N. A. M. Zabidi, R. M. Ramli and N. A. Suhaimi, The Activity and Stability of Promoted Cu/ZnO/Al_2O_3 Catalyst for CO_2 Hydrogenation to Methanol, *Processes*, 2023, **11**, 719, DOI: 10.3390/pr11030719.

11 M. Pori, I. Arčon, V. D. B. C. Dasireddy, B. Likozar, Z. C. Orel and M. Marinšek, Photo-Chemically-Deposited and Industrial Cu/ZnO/Al_2O_3 Catalyst Material Surface Structures During CO_2 Hydrogenation to Methanol: EXAFS, XANES and XPS Analyses of Phases After Oxidation, Reduction, and Reaction, *Catal. Lett.*, 2021, **151**, 3114–3134, DOI: 10.1007/s10562-021-03556-1.

12 H. M. Al-Attar, H. T. Hussein, R. S. Zamel, A. J. Addie and M. K. A. Mohammed, Methylene blue degradation using ZnO:CuO:Al_2O_3 nanocomposite synthesized by liquid laser ablation, *Opt. Quantum Electron.*, 2023, **55**, 309, DOI: 10.1007/s11082-023-04597-z.

13 N. H. Berahim, N. A. Mohd Zabidi and N. A. Suhaimi, Co-Production of Methanol and Methyl Formate *via* Catalytic Hydrogenation of CO_2 over Promoted Cu/ZnO Catalyst Supported on Al_2O_3 and SBA-15, *Catalysts*, 2022, **12**, 1018, DOI: 10.3390/catal12091018.

14 I. I. Maor, S. Heyte, O. Elishav, M. Mann-Lahav, J. Thuriot-Roukos, S. Paul and G. S. Grader, Performance of Cu/ZnO Nanosheets on Electrospun Al_2O_3 Nanofibers in CO_2 Catalytic Hydrogenation to Methanol and Dimethyl Ether, *Nanomaterials*, 2023, **13**, 635, DOI: 10.3390/nano13040635.

15 H. Ajamein, M. Haghighi, S. Minaei and S. Alaei, Texture/phase evolution during microwave fabrication of nanocrystalline multicomponent (Cu/Zn/Al) O metal oxides with varying diethylene glycol content applied in hydrogen production, *Int. J. Hydrogen Energy*, 2018, **43**, 22838–22851, DOI: 10.1016/j.ijhydene.2018.10.174.

16 T. Kamsuwan, C. Krutpijit, S. Praserthdam, S. Phatanasri, B. Jongsomjit and P. Praserthdam, Comparative study on the effect of different copper loading on catalytic behaviors and activity of Cu/ZnO/Al_2O_3 catalysts toward CO and CO_2 hydrogenation, *Heliyon*, 2021, **7**, e07682, DOI: 10.1016/j.heliyon.2021.e07682.

17 Z. Sakhaei and M. Rezaei, Mechanochemical synthesis of ZnO. Al_2O_3 powders with various Zn/Al molar ratios and their applications in reverse water-gas shift reaction, *Environ. Sci. Pollut. Res.*, 2021, **28**, 13790–13799, DOI: 10.1007/s11356-020-11536-y.

18 Y. Li and J. Z. Zhang, Hydrogen generation from photoelectrochemical water splitting based on nanomaterials, *Laser Photonics Rev.*, 2010, **4**, 517–528, DOI: 10.1002/lpor.200910025.

19 A. M. Abdelghany, A. M. Sarhan, E. Abdel-Latif and F. I. El-Dossoki, Synthesis and characterization of CuO/ZnO/Al_2O_3 particles and its utilization as a catalyst for acrylamide derivatives, *J. Mol. Struct.*, 2021, 1241, DOI: 10.1016/j.molstruc.2021.130664.

20 A. M. Al-Mohaimeed, G. A. E. Mostafa and M. F. El-Tohamy, New construction of functionalized CuO/Al_2O_3 nanocomposite-based polymeric sensor for potentiometric estimation of naltrexone hydrochloride in commercial formulations, *Polymers*, 2021, **13**, 4459, DOI: 10.3390/polym13244459.

21 A. Nasirian, Synthesis and characterization of Cu nanoparticles and studying of their catalytic properties Archive of SID Synthesis and characterization of Cu nanoparticles and studying of their catalytic properties, *Int. J. Nano Dimens.*, 2012, **2**, 159–164, DOI: 10.7508/ijnd.2011.03.002.

22 I. Ahmad, S. Shukrullah, M. Y. Naz, M. A. Rasheed, M. Ahmad, E. Ahmed, M. S. Akhtar, N. R. Khalid, A. Hussain and S. Khalid, Boosted hydrogen evolution activity from Sr doped ZnO/CNTs nanocomposite as visible light driven photocatalyst, *Int. J. Hydrogen Energy*, 2021, **46**, 26711–26724, DOI: 10.1016/j.ijhydene.2021.05.164.

23 I. Ahmad, R. Bousbih, A. Mahal, W. Q. Khan, M. Aljohani, M. A. Amin, N. N. A. Jafar, M. S. Jabir, H. Majdi, A. S. Alshomrany, M. Shaban, I. Ali and H. Bayahia, Recent progress in ZnO-based heterostructured photocatalysts: A review, *Mater. Sci. Semicond. Process.*, 2024, **180**, 108578, DOI: 10.1016/j.mssp.2024.108578.

24 Y. Yang, K. Pan, S. Wei, W. Li, L. Xu, J. Li, F. Xiao, X. Wu, Q. Li, S. Guo and Y. Yang, Hydrothermal synthesis and adsorption property of porous spherical Al_2O_3 nanoparticles, *Mater. Res. Express*, 2019, **6**, 075023, DOI: 10.1088/2053-1591/ab1372.

25 A. Sanni, D. Govindarajan, S. Nijpanich, W. Limphirat, M. Tipplook, K. Teshima, S. Sangaraju and S. Kheawhom, Designing dual-phase ZnO–Al_2O_3–CuO nanostructures for enhanced supercapacitor performance, *Mater. Res. Bull.*, 2025, **189**, 113443, DOI: 10.1016/j.materresbull.2025.113443.

26 Y. Li, C. Luo and Q. Su, Performance of Cu/ZnO/Al_2O_3 Catalysts Prepared by Sol–Gel Methods on Methanol Steam Reforming, *Energies*, 2023, **16**, 7803, DOI: 10.3390/en16237803.

27 S. B. Bagherzadeh and M. Haghighi, Plasma-enhanced comparative hydrothermal and coprecipitation preparation of CuO/ZnO/Al_2O_3 nanocatalyst used in hydrogen production via methanol steam reforming, *Energy Convers. Manage.*, 2017, **142**, 452–465, DOI: 10.1016/j.enconman.2017.03.069.

28 R. Shokrani, M. Haghighi, H. Ajamein and M. Abdollahifar, Hybrid sonochemic urea-nitrate combustion preparation of CuO/ZnO/Al_2O_3 nanocatalyst used in fuel cell-grade hydrogen production from methanol: Effect of sonication and fuel/nitrate ratio, *Part. Sci. Technol.*, 2018, **36**, 217–225, DOI: 10.1080/02726351.2016.1241846.

29 H. Ajamein, M. Haghighi and S. Alaei, The role of various fuels on microwave-enhanced combustion synthesis of CuO/ZnO/Al_2O_3 nanocatalyst used in hydrogen production via methanol steam reforming, *Energy Convers. Manage.*, 2017, **137**, 61–73, DOI: 10.1016/j.enconman.2017.01.044.

30 H. Ajamein and M. Haghighi, Influence of ambient gas on microwave-assisted combustion synthesis of CuO–ZnO–Al_2O_3 nanocatalyst used in fuel cell grade hydrogen production via methanol steam reforming, *Ceram. Int.*, 2016, **42**, 17978–17989, DOI: 10.1016/j.ceramint.2016.07.092.

31 H. Vafaee Zonouz, F. Barzegari and M. Rezaei, Development of CuO/ZnO/Al_2O_3-hydrotalcite – based catalysts for middle temperature water gas shift reaction: Impact of calcination temperature and residual carbonates, *Fuel*, 2024, **378**, 132882, DOI: 10.1016/j.fuel.2024.132882.

32 C. Baltes, S. Vukojević and F. Schüth, Correlations between synthesis, precursor, and catalyst structure and activity of a large set of CuO/ZnO/Al_2O_3 catalysts for methanol synthesis, *J. Catal.*, 2008, **258**, 334–344, DOI: 10.1016/j.jcat.2008.07.004.

33 H. G. El-Shobaky, M. Mokhtar and G. A. El-Shobaky, Physicochemical surface and catalytic properties of CuO ± ZnO/Al_2O_3 system, *Appl. Catal., A*, 1999, **180**, 335–344, DOI: 10.1016/S0926-860X(98)00357-3.

34 N. Saafie, S. Sufian, N. Mufti and M. F. R. Samsudin, The role of g-C_3N_4 loadings in MXene for photocatalytic degradation of methylene blue, *J. Mater. Sci.: Mater. Electron.*, 2025, **36**, 389, DOI: 10.1007/s10854-025-14395-w.

35 N. A. Razali and S. A. Othman, The morphology characterization of nitrogen and magnesium doped with titanium dioxide (TiO_2) using field emission scanning electron

(FESEM) for photocatalytic study, *Int. J. Emerg. Trends Eng. Res.*, 2020, **8**, 108–111, DOI: 10.30534/ijeter/2020/1581.22020.

36 T. T. Nguyen, J. Balamurugan, N. H. Kim and J. H. Lee, Hierarchical 3D Zn–Ni–P nanosheet arrays as an advanced electrode for high-performance all-solid-state asymmetric supercapacitors, *J. Mater. Chem. A*, 2018, **6**, 8669–8681, DOI: 10.1039/c8ta01184b.

37 M. Mousavi-Kamazani, Facile sonochemical-assisted synthesis of Cu/ZnO/Al_2O_3 nanocomposites under vacuum: Optical and photocatalytic studies, *Ultrason. Sonochem.*, 2019, **58**, 104636, DOI: 10.1016/j.ultsonch.2019.104636.

38 A. Zhang, W. Zheng, Z. Yuan, J. Tian, L. Yue, R. Zheng, D. Wei and J. Liu, Hierarchical NiMn-layered double hydroxides@CuO core–shell heterostructure in-situ generated on Cu $(OH)_2$ nanorod arrays for high performance supercapacitors, *Chem. Eng. J.*, 2020, **380**, 122486, DOI: 10.1016/j.cej.2019.122486.

39 H. M. Al-Attar, H. T. Hussein, R. S. Zamel and A. J. Addie, and M. K. A. Mohammed, Methylene blue degradation using ZnO:CuO:Al_2O_3 nanocomposite synthesized by liquid laser ablation, *Opt. Quantum Electron.*, 2023, **56**, 309, DOI: 10.1007/s11082-023-04597-z.

40 C. Chang, C. Y. Lee and N. H. Tai, Human Exhalation CO_2 Sensor Based on the PEI-PEG/ZnO/NUNCD/Si Heterojunction Electrode, *ACS Omega*, 2022, **7**, 15657–15665, DOI: 10.1021/acsomega.2c00479.

41 K. Soumya, I. P. Selvam, C. P. Vinod and S. N. Potty, Tuning of work function of ZnO by doping and co-doping: An investigation using X-ray photoelectron spectroscopy, *Thin Solid Films*, 2022, **761**, 139538, DOI: 10.1016/j.tsf.2022.139538.

42 G. Ma, W. Tang, A. Wang, L. Zhang, J. Guan, N. Han and Y. Chen, Heterojunctioned CuO/Cu_2O catalyst for highly efficient ozone removal, *J. Environ. Sci.*, 2023, **125**, 340–348, DOI: 10.1016/j.jes.2022.01.032.

43 S. M. Kim, A. Armutlulu, W. C. Liao, D. Hosseini, D. Stoian, Z. Chen, P. M. Abdala, C. Copéret and C. Müller, Structural insight into an atomic layer deposition (ALD) grown Al_2O_3 layer on Ni/SiO_2: Impact on catalytic activity and stability in dry reforming of methane, *Catal. Sci. Technol.*, 2021, **11**, 7563–7577, DOI: 10.1039/d1cy01149a.